The roles of equatorial trapped waves and internal inertia-gravity waves in driving the quasi-biennial oscillation.
Part II: three-dimensional distribution of wave forcing

Yoshio Kawatani
Japan Agency for Marine-Earth Science and Technology, Yokohama, Japan

Kaoru Sato
Department of Earth and Planetary Science, Graduate School of Science, University of Tokyo, Tokyo, Japan

Timothy J. Dunkerton
Northwest Research Associates, Redmond, WA, USA

Shingo Watanabe
Japan Agency for Marine-Earth Science and Technology, Yokohama, Japan

Saburo Miyahara
Department of Earth and Planetary Sciences, Graduate School of Sciences, Kyushu University, Fukuoka, Japan

Masaaki Takahashi
Center for Climate System Research, University of Tokyo, Kashiwa, Japan

_____
[1]*Corresponding author address:* Yoshio Kawatani, Japan Agency for Marine-Earth Science and Technology, Yokohama, 236-0001, Japan
E-mail: yoskawatani@jamstec.go.jp

Abstract

Three-dimensional wave forcing of simulated quasi-biennial oscillation (QBO) is investigated using a high-resolution atmospheric general circulation model with T213L256 resolution (60-km horizontal and 300-m vertical resolution). In both the eastward and westward wind shear phases of the QBO, nearly all Eliassen–Palm flux (EP-flux) divergence due to internal inertia-gravity waves (defined as fluctuations with zonal wavenumber ≥ 12) results from the divergence of the vertical component of the flux. On the other hand, EP-flux divergence due to equatorial trapped waves (EQWs) results from both the meridional and vertical components of the flux in regions of strong vertical wind shear. Longitudinal dependence of wave forcing is also investigated by three-dimensional wave activity flux applicable to gravity waves. Near the top of the Walker circulation, strong eastward (westward) wave forcing occurs in the Eastern (Western) Hemisphere due to internal inertia-gravity waves with small horizontal phase speed. In the eastward wind shear zone associated with the QBO, the eastward wave forcing due to internal inertia-gravity waves in the Eastern Hemisphere is much larger than that in the Western Hemisphere, whereas in the westward wind shear zone, westward wave forcing does not vary much in the zonal direction. Zonal variation of wave forcing in the stratosphere results from (1) zonal variation of wave sources, (2) the vertically sheared zonal winds associated with the Walker circulation, and (3) the phase of the QBO.

1. Introduction

Ground-based observational instruments such as radiosondes, rockets, and radar are used to study atmospheric waves. Intensive or periodic observations with fine vertical resolution have revealed characteristics of gravity waves in the tropical region (e.g., Tsuda *et al.* 1994; Maruyama 1994; Sato *et al.* 1994; Sato and Dunkerton 1997; Wada *et al.* 1999). Radiosonde observations have revealed that momentum transported by short-period ($\leq$~3 days) gravity waves is comparable to that transported by long-period Kelvin waves (Maruyama 1994; Sato and Dunkerton 1997). Ground-based measurements of wind components can provide information on momentum flux, but most observation points are located on land. Because mean wind distributions and tropospheric cumulus convection activities are not zonally uniform in equatorial regions, gravity waves propagating upward into the stratosphere are not zonally uniform (Bergman and Salby 1994). Satellite-based instruments have the advantage of observing gravity waves globally (e.g., Tsuda *et al.* 2000, 2009; Ratnam *et al.* 2004; Randel and Wu 2005; Ern *et al.* 2008; Alexander *et al.* 2008a, b). However, satellite data allow calculation of temperature but not of wind components in the equatorial lower stratosphere, and the analyzable spatial and temporal spectrum is limited.

The relatively small temporal and spatial scales of gravity waves preclude comprehensive investigations of gravity waves over a wide geographic range using only observational data. Atmospheric general circulation models (AGCMs) are effective tools with which to study the characteristics of gravity waves, including their global propagation, momentum fluxes, and wave forcing on mean flows (e.g., Sato *et al.* 1999,

2009; Kawatani *et al.* 2003, 2004, 2005, 2009, 2010; Watanabe *et al.* 2005, 2006, 2008; Watanabe 2008).

Kawatani *et al.* (2005) simulated a QBO-like oscillation in a T106L60 AGCM without gravity wave drag parameterization (for simplicity, we refer to the QBO-like oscillation as the QBO hereafter). They demonstrated a zonally non-uniform distribution of the vertical flux of the zonal momentum ($\overline{u'w'}$) of internal inertia-gravity waves (for simplicity, referred to hereafter as "internal gravity waves") with periods ≤3 days in the upper troposphere. They also indicated that the vertical divergence of $\overline{u'w'}$ (i.e., $\partial(\overline{u'w'})/\partial z$; z denotes the altitude) due to internal gravity waves in the Eastern Hemisphere was much greater than that in the Western Hemisphere at the altitude where the phase of the QBO changed from westward to eastward wind. However, Kawatani *et al.* (2005) analyzed data from 2 months during only the eastward wind shear phase of the QBO and did not investigate wave forcing during the westward wind shear phase. They also did not study wave forcing associated with equatorial trapped waves (EQWs).

Kawatani *et al.* (2009) examined the global distribution, sources, and propagation of EQWs and internal gravity waves using the T106L60 AGCM. The purpose of that study was to clarify the mechanism of the global distribution of EQWs and internal gravity waves in comparison with results from recent satellite observations. Potential energy $[= 1/2\,(g/N)^2 \overline{\left(T'/\overline{T}\right)^2}$, where *g*, *N*, and *T* are the gravitational acceleration, buoyancy frequency, and temperature, respectively, and the overbar denotes the background mean field] is often used as an indicator of the global distribution of EQWs and internal gravity waves in studies based on satellite data because potential energy can be calculated from observed temperature alone. Therefore, Kawatani *et al.* (2009)

investigated the global distribution of simulated wave potential energy. Each EQW generation generally corresponded well with the source of each convectively coupled EQW activity in the troposphere. The difference in the vertical shear of the Walker circulation between the Eastern and Western hemispheres plays an important role in wave filtering, which results in zonally different wave potential energy distributions in the upper troposphere and lower stratosphere (UTLS) region. The model results were essentially consistent with recent results obtained from GPS radio occultation (RO) data (Alexander *et al.* 2008b; Tsuda *et al.* 2009). However, Kawatani *et al.* (2009) did not study wave momentum flux and wave forcing.

In estimating wave forcing, meridional momentum transport by EQWs has not always been considered (e.g., Tindall *et al.* 2006a, b). For Kelvin waves, only the $\overline{u'w'}$ term has been estimated as wave momentum flux to study the possible role of Kelvin waves in driving the QBO (e.g., Sato and Dunkerton 1997; Ern and Preusse 2009). Recently, Imamura (2006) investigated meridional propagations of EQWs in the Venusian middle atmosphere and reported that meridional transport of momentum flux by EQWs plays important roles in maintaining the super-rotation in Venus' atmosphere [see Imamura (2006) for more details of the Venusian atmosphere]. In part I of this study, Kawatani *et al.* (2010) investigated the roles of EQWs and internal gravity waves in driving the simulated QBO in zonal mean and meridionally averaged fields from 10ºN to 10ºS using the T213L256 AGCM. Here in part II, we describe the meridional distributions of zonal wave forcing due to Earth's EQWs around the QBO shear zones.

Most previous studies have discussed wave forcing in a zonal-mean field, which seems to be appropriate because the QBO is a nearly zonally uniform phenomenon. In

fact, the stratospheric QBO has longitudinal variation, as discussed by Hamilton *et al.* (2004). Because wave generation and propagation depend greatly on zonal direction (Alexander *et al.* 2008a, b; Kawatani *et al.* 2009), wave forcing should vary zonally. Model investigations of the three-dimensional (3-D) distribution of wave momentum flux and wave forcing should provide useful information for future *in situ* and satellite observations, as well as for the development of gravity wave parameterizations (see McLandress 1998 and references therein).

In this study, we first describe the zonal-mean meridional distributions of zonal wave forcing due to EQWs and internal gravity waves around the QBO shear zones using outputs from the T213L256 AGCM. Second, we focus on the longitudinal distributions of wave forcing. To investigate wave activity in detail, two representative time periods are selected: July of the first year, during the eastward wind shear, and January of the second year, during the westward wind shear phase of the QBO (see Fig. 1a in part I of this paper). Part I of this paper describes the model. This paper is arranged as follows. Section 2 discusses the validation of wave momentum flux. Section 3 examines the meridional distribution of zonal wave forcing. Section 4 describes the longitudinal dependence of wave forcing. Section 5 summarizes the study and provides concluding remarks.

2. Validation of wave momentum flux

First, the validation of simulated momentum flux is discussed to check the realism of the model. Sato and Dunkerton (1997) analyzed twice-daily rawinsonde data measured at Singapore (1.4°N, 104°E) and estimated the net momentum flux $\overline{u'w'}$ and the absolute value of $|\overline{u'w'}|$ for 1- to 3-day period components (the overbar denotes the time mean).

Net $\overline{u'w'}$ is composed of positive $(\overline{u'w'})_+$ and negative $(\overline{u'w'})_-$ momentum flux, and $|\overline{u'w'}|$ is the sum of the absolute values of $\overline{u'w'}$ as follows:

$$\overline{u'w'} \equiv (\overline{u'w'})_+ + (\overline{u'w'})_- ,\qquad(1)$$

$$|\overline{u'w'}| \equiv |(\overline{u'w'})_+| + |(\overline{u'w'})_-| .\qquad(2)$$

In Sato and Dunkerton's (1997) study, momentum flux was estimated at the altitude where the absolute value of the mean zonal wind $|\bar{u}|$ was smaller than 5 m s^{-1} in the eastward wind/westward wind shear of the QBO. In the eastward wind shear phase, $|\overline{u'w'}|$ was 20–60 x 10^{-3} m^2 s^{-2}, whereas $\overline{u'w'}$ was only 0 to +4 x 10^{-3} m^2 s^{-2}. In the westward wind shear, $|\overline{u'w'}|$ was 10–30 x 10^{-3} m^2 s^{-2}, whereas $\overline{u'w'}$ was almost zero. The discrepancy between $\overline{u'w'}$ and $|\overline{u'w'}|$ indicated a large cancellation between positive and negative momentum fluxes.

Before comparing the rawinsonde observations with the present model results, two issues should be noted. First, if aliasing from higher frequency waves is present (with periods shorter than 1 day for twice-daily rawinsonde data), the actual momentum flux should be larger. Second, gravity waves with much longer vertical wavelength (λ_z) may not be recognized in rawinsonde observations. In the eastward (westward) shear phase, eastward (westward) propagating gravity waves having small intrinsic phase speeds and hence small λz are preferably observed by rawinsondes (see Baldwin *et al.* 2001 for more details).

Figure 1 shows longitude–height cross sections of $\overline{u'w'}$ and $|\overline{u'w'}|$ in July during Fig.1 the eastward wind shear phase and January during the westward wind shear phase of the QBO. To compare simulated momentum fluxes with those reported by Sato and

Dunkerton (1997), $\overline{u'w'}$ values with periods ≤3 days averaged from 3°S–3°N are shown (one latitudinal grid at 1.4°N was not selected, but the $\overline{u'w'}$ at 1.4°N is nearly equal to that at 3°S–3°N). The dashed vertical line corresponds to the location of Singapore. In the eastward wind shear, $\overline{u'w'}$ and $|\overline{u'w'}|$ over Singapore are +10 x 10^{-3} m^2 s^{-2} and 26 x 10^{-3} m^2 s^{-2} at the altitude of $|\bar{u}| \leq 5$ m s^{-1} (~35 hPa), respectively. On the other hand, these fluxes in the westward wind shear are -10 x 10^{-3} m^2 s^{-2} and 23 x 10^{-3} m^2 s^{-2} around 30 hPa. Taking into account the aliasing and observable λz in rawinsonde observations, eastward gravity waves would be reasonably simulated. On the other hand, westward gravity waves would be slightly overestimated.

Sato and Dunkerton (1997) also estimated net $\overline{u'w'}$ with a period from 5 to 20 days (which they assumed to be Kelvin waves) in the eastward wind shear to be +2–9 x 10^{-3} m^2 s^{-2}, whereas simulated net $\overline{u'w'}$ with a period from 5 to 20 days in this study is estimated to be ~+3 x 10^{-3} m^2 s^{-2} (not shown). To investigate momentum flux associated with EQWs, an equatorial wave filter was applied to physical quantities such as temperature, wind, and geopotential height. In this study, each EQW component is defined as waves that satisfy the dispersion curves of each EQW with 2 m $\leq h_e \leq$ 90 m (h_e is the equivalent depth), s $\leq$ 11, and periods ≥1.1 days (see Figs. 5e, f of part I for more details). The net $\overline{u'w'}$ associated with Kelvin waves extracted by the equatorial wave filter in the eastward wind shear is ~+4.5 x 10^{-3} m^2 s^{-2} (not shown). These results indicate that the model also well simulated the momentum fluxes associated with Kelvin waves as well as their amplitude, which appeared in temperature disturbances (as mentioned in part I).

An important point from Fig. 1 is that the model reveals strong longitudinal variation in both $\overline{u'w'} \le 3$ day and $|\overline{u'w'}| \le 3$ day. The values of positive $\overline{u'w'}$ are much larger in the Eastern Hemisphere than in the Western Hemisphere during the eastward wind shear phase, as indicated by Kawatani *et al.* (2005). On the other hand, negative $\overline{u'w'}$ is slightly larger in the Western Hemisphere than in the Eastern Hemisphere during the westward wind shear phase. The model results indicate that the wave momentum fluxes observed at Singapore by Sato and Dunkerton (1997) would have been larger than the zonal mean fluxes. Section 4 will present a detailed discussion of the zonal variation of wave forcing.

3: Meridional distribution of zonal wave forcing

Part I of this study discusses the zonal-mean wave forcing due to EQWs and internal gravity waves in the 10ºN–10ºS averaged field. In this section, we focus on the zonal-mean meridional distribution of wave forcing around eastward/westward wind shear zones of the QBO.

The Eliassen–Palm (EP-flux) is used to analyze wave propagation and zonal wave forcing in the meridional plane of zonal-mean zonal wind, defined as follows (Andrews *et al.* 1987):

$$F^{(\phi)} = \rho_0 a \cos\phi \left(\overline{u_z} \, \overline{v'\theta'} / \overline{\theta_z} - \overline{u'v'} \right) , \tag{3}$$

$$F^{(z)} = \rho_0 a \cos\phi \left\{ \left[f - (a\cos\phi)^{-1} \left(\overline{u}\cos\phi \right)_\phi \right] \overline{v'\theta'} / \overline{\theta}_z - \overline{u'w'} \right\}, \tag{4}$$

$$\nabla \cdot \mathbf{F} = (a\cos\phi)^{-1} \partial/\partial\phi \left(F^{(\phi)} \cos\phi \right) + \partial F^{(z)} / \partial z . \tag{5}$$

In the above equations, ρ_0, a, ϕ, z, u, v, w, θ, and f are the log-pressure height dependent density, mean radius of the earth, latitude, log-pressure height, zonal wind, meridional wind, vertical wind, potential temperature, and Coriolis parameter ($f \equiv 2\Omega\sin\phi$, where Ω is the rotation rate of the Earth), respectively. The subscripts ϕ, z, and t denote a meridional, vertical, and time derivative, respectively. Eastward and westward wave forcing corresponds to the EP-flux divergence and convergence (i.e., $\nabla \cdot \mathbf{F} > 0$ and $\nabla \cdot \mathbf{F} < 0$), respectively.

Figure 2 presents a latitude–height cross section of the EP-flux and its divergence | Fig. 2 due to s ≤ 11 and s ≥ 12 waves in July during the eastward wind shear phase and in January during the westward wind shear phase of the QBO. Vertical profiles of EP-flux divergence due to the vertical and meridional component of the flux averaged from 10°S to 10°N are shown in the right panels. Waves with s ≤ 11 include EQWs, large-scale gravity waves, tides, and extra-tropical Rossby waves. In the eastward wind shear, large downward EP-flux with s ≤ 11 dominates around the equator, resulting in eastward wave forcing around 45–30 hPa (Fig. 2a), whereas in the westward shear, the EP-flux with s ≤ 11 and its divergence are small (Fig. 2d). In the winter hemisphere (i.e., Southern Hemisphere in July and Northern Hemisphere in January), meridional components of the EP-flux are apparent. As discussed in part I of this paper, these fluxes are due to extra-tropical Rossby waves propagating from the winter hemisphere to the equatorial region.

In this study, fluctuations with s ≥ 12 are considered to be internal gravity waves (see section 4 in part I of this paper). The internal gravity wave forcing in July and January is not symmetrically distributed around the equator (Figs. 2b, e), which would mainly result from annual variation of zonal mean flows. The wave forcing distribution in

April and October becomes much more symmetric compared to that in January and July due to more symmetric distribution of background zonal wind (now shown). If annual cycles are removed, the distribution of wave forcing and background zonal wind becomes more symmetric in relation to the equator (Giorgetta *et al.* 2006). The interannual variation of the QBO and wave forcing is beyond the scope of this study, in which the model was integrated for only 3 years.

In both the eastward and westward wind shear phases, nearly all EP-flux divergence due to internal gravity waves results from the divergence of the vertical component of the flux, while that of the meridional component is negligible (Figs. 2c, f). Further investigation reveals that the divergence mainly results from the term containing the vertical flux of zonal momentum [$\overline{u'w'}$; second term of Eq. (4)]. In lower resolution GCMs, gravity wave drag parameterization is sometimes used to obtain the QBO (Giorgetta *et al.* 2002, 2006). Gravity wave drag parameterization generally considers waves propagating in only the vertical direction. The present model result indicates that gravity wave drag parameterization including only vertical wave propagation is suitable, at least for the simulation of the QBO; however, seasonal and annual variations of the wave-source distribution remain a problem for gravity wave drag parameterization. Meridional propagation of gravity waves is more important for wave forcing in the mid- to high latitudes (Watanabe 2008; Sato *et al.* 2009).

Next, meridional and vertical momentum transport by EQWs is discussed. Here, meridional and vertical propagations of Kelvin waves, n = 0 EIGWs (n is the order of solution for the equatorial wave mode, see Eq. (8) in part I of this study; eastward- and westward-propagating inertia-gravity waves are referred to as EIGWs and WIGWs,

respectively), and mixed Rossby-gravity (MRG) waves in relation to the vertical shear of the QBO are investigated because these waves induce relatively large zonal wave forcing among EQWs during the time periods analyzed in part I.

Figure 3 shows the latitude–height cross section of the EP-flux and its divergence $\boxed{\text{Fig. 3}}$ due to Kelvin waves and n = 0 EIGWs in July during the eastward wind shear phase and MRG waves in January during the westward wind shear phase of the QBO. EP-flux divergence due to vertical and meridional components of the flux is also shown separately. In both periods, the meridional wind is negligibly smaller than the zonal wind around the QBO shear zones (not shown).

Kelvin waves in the lower stratosphere propagate upward around ~15°N–15°S with their maximum $F^{(z)}$ over the equator (Fig. 3a). They converge in both meridional and vertical directions in the eastward wind shear zones, resulting in large eastward wave forcing around 45–25 hPa. Eastward wave forcing associated with vertical components of the EP-flux is distributed widely in both the meridional and vertical domains (Fig. 3g). On the other hand, meridional components of the EP-flux induce large eastward wave forcing around the equator and weak westward wave forcing off the equator (Fig. 3d). Consequently, larger eastward wave forcing is concentrated on the equator in comparison to the case considering the vertical components only. In the 10°S–10°N averaged field, ~85% of the EP-flux divergence is explained by the divergence of the vertical components of the flux, and ~15% is explained by that of the meridional components around 35 hPa.

In the lower stratosphere, n = 0 EIGWs propagate upward with their maximum $F^{(z)}$ off the equator around 6°S and 6°N (Fig. 3b). In the eastward wind shear zones,

eastward wave forcing occurs off the equator, whereas westward wave forcing occurs over the equator. In the 10°S–10°N averaged field, EP-flux divergence from the meridional component of the flux is much smaller than that from the vertical component due to cancelation between eastward wave forcing off the equator and westward wave forcing over the equator. Consequently, n = 0 EIGWs make the zonal wind of the QBO eastward in the 10°S–10°N mean field.

MRG waves propagate upward in the lower stratosphere, with their maximum $F^{(z)}$ off the equator, and converge both meridionally and vertically in the westward wind shear zones (Fig. 3c). Westward wave forcing due to the vertical component of the EP-flux is found off the equator (Fig. 3i). The ratio of this westward wave forcing between the first ($\overline{v'\theta'}$ term) and second ($\overline{u'w'}$ term) terms of $F^{(z)}$ [see Eq. (4)] is approximately -2 (westward wave forcing) versus 1 (eastward wave forcing), which is consistent with the theoretical estimation (not shown; the phase structure of a MRG wave is illustrated in Fig. 4.21 of Andrews *et al.* 1987). Thus, EP-flux divergence from the vertical component of the flux results in westward wave forcing. As mentioned in part I of this study, the amplitude of temperature disturbances associated with simulated MRG waves is ~1.2 K, which is also consistent with recent satellite observations (Ern *et al.* 2008; Alexander *et al.* 2008b). Because MRG waves focus equatorward in the westward wind shear zones, and strong meridional momentum transport occurs around the equator, westward wave forcing is maximized around the equator.

The existence of local westward wave forcing near the equator by n=0 mode was indicated in a theoretical study by Andrews and McIntyre (1976) and in the numerical solutions reported by Imamura (2006). The meridional–vertical distribution of the EP-

flux and its divergence due to Kelvin waves, n = 0 EIGWs, and MRG waves are similar to numerical solutions by Imamura (2006), although they investigated the EQW propagation under the middle atmosphere of Venus. The present analysis reveals that the wave-forcing distribution varies strongly in the meridional direction and indicates that the meridional momentum transport, as well as the vertical transport, by EQWs should be considered when investigating the contributions of EQWs to driving the QBO. However, how EQW motions in realistic 3-D background winds affect the EP-flux has not yet been well established (cf. Tindall *et al.* 2006b). More theoretical studies and numerical experiments of wave motions in a realistic 3-D background associated with the QBO are needed to understand and generalize EQW propagation, which is beyond the scope of the present study.

Figure 4 shows the latitudinal distribution of the EP-flux divergence at 45–25 hPa | Fig.4 | in July during the eastward wind shear phase and at 35–20 hPa in January during the westward wind shear phase of the QBO. These altitude ranges were selected based on the distribution of strong wave forcing (Fig. 2). As described in the figure caption, large-scale non-EQW components are defined as waves with $s \leq 11$ that do not satisfy the dispersion curves of EQWs with $2 \leq h_e \leq 90$ m (see section 4 of part I). In the eastward wind shear phase (Fig. 4a), eastward wave forcing due to the odd mode of eastward EQWs (i.e., Kelvin waves and n = 1 EIGWs; line A) is confined around the equator. Zonal wave forcing due to n = 0 and n = 2 EIGWs (line B) is eastward off the equator but westward over the equator. Consequently, eastward wave forcing due to eastward EQWs (line C) is ~2.0 x 10^{-1} m s^{-1} day^{-1} over the equator. Zonal wave forcing due to internal gravity waves (line E) is comparable to that due to eastward EQWs over the equator and

prevails off the equator. Consequently, EQWs contribute to ~38% of total wave forcing in the 10°S–10°N and 45–25 hPa averaged field.

In the westward wind shear phase (Fig. 4b), westward wave forcing due to internal gravity waves (line E) is -3.5 x 10^{-1} m s^{-1} day^{-1}, whereas that due to westward EQWs (line A + B + C) reaches up to -0.7 x 10^{-1} m s^{-1} day^{-1} over the equator. Thus, the westward EQWs explain ~17% of total wave forcing over the equator, but the contribution of these waves is reduced to ~8% in the 10°S–10°N averaged field. Westward wave forcing due to MRG waves is largest among the EQWs. The zonal wave forcing by n = 1 / n = 2 WIGWs and equatorial Rossby waves is negligible during this time period. Large westward wave forcing due to large-scale non-EQWs (line D) is obvious in the Northern Hemisphere. The EP-flux due to large-scale non-EQWs indicates that this wave forcing is mainly due to the propagation of extratropical Rossby waves from the winter hemisphere into the equatorial region (not shown).

4. Longitudinal dependence of wave forcing

4.1. Three-dimensional wave activity flux applicable to inertia-gravity waves

In this section, we turn our attention to the longitudinal dependence of wave forcing. We also discuss the influence of tropospheric wave sources and tropospheric circulations on the distribution of wave forcing in the stratosphere.

First, horizontal maps of precipitation in July and January obtained by observations and by the model are shown in Fig. 5. The observational data are Climate Prediction Center (CPC) Merged Analysis of Precipitation (CMAP; Xie and Arkin 1996) data averaged from 1979 to 2001. The model results are from July of the first year and

Fig.5

January of the second year. The observations represent the climatology, whereas the model results are from only 1 year. Therefore, we cannot directly compare the model and observation results. However, the model reasonably simulated the spatial distribution of precipitation, such as the strong precipitation over the Indian monsoon region in July, the large precipitation areas around or to the south of the equator from the Indian Ocean to the mid-Pacific in January, the separation between the Intertropical Convergence Zone (ITCZ) and the South Pacific Convergence Zone (SPCZ), and the strong precipitation over Africa and South America. Watanabe *et al.* (2008) also compared the amount of simulated precipitation to that in observations. They indicated that the present AGCM slightly overestimated the zonal-mean precipitation near the equator and in the mid-latitudes of both hemispheres, but by less than 1 σ.

As reported in part I of this study, the model well simulated spectral signals of convectively coupled EQWs in the zonal wavenumber / frequency domain (see Fig. 4 in part I). The global distributions of simulated convectively coupled EQWs were found to be similar to those in the real atmosphere. Kawatani *et al.* (2009) showed that the global distributions and strengths of convectively coupled EQWs were well simulated in the same model except for at lower (T106L60) resolutions (see Fig. 9 of their study).

Kawatani *et al.* (2009) used energy flux to investigate global wave propagation in a 3-D domain. The energy flux is useful to investigate 3-D wave propagation and to clarify the mechanism of the global wave energy distribution discovered by satellite observations (Kawatani *et al.* 2003, 2009; Alexander *et al.* 2008a). However, the energy flux cannot be used to understand the 3-D wave forcing distribution (Gill 1982).

Recently, Miyahara (2006) derived 3-D wave activity flux applicable to inertia-gravity waves (hereafter referred to as 3-D wave flux). The 3-D wave flux related to zonal wave forcing in the log-pressure coordinate system on spherical geometry is defined as follows:

$$\frac{D\bar{u}}{Dt} - \frac{\bar{u}\tan\phi}{a}\bar{v} - 2\Omega\sin\phi\bar{v}^{*} = -\frac{1}{a\cos\phi}\frac{\partial\overline{\Phi}}{\partial\lambda} - \left(pa\cos\phi\right)^{-1}\left(\nabla\cdot\mathbf{F}\right)_{3D}, \tag{6}$$

$$\left(\nabla\cdot\mathbf{F}\right)_{3D} = \frac{1}{a\cos\phi}\frac{\partial(F_{3D}^{(\lambda)})}{\partial\lambda} + \frac{1}{a\cos\phi}\frac{\partial(F_{3D}^{(\phi)}\cos\phi)}{\partial\phi} + \frac{\partial(F_{3D}^{(z)})}{\partial z}, \tag{7}$$

$$(F_{3D}^{(\lambda)}, F_{3D}^{(\phi)}, F_{3D}^{(z)}) = (\frac{1}{2}(\overline{u'^2} - \overline{v'^2} + \frac{\overline{\Phi_z'^2}}{N^2}), \overline{u'v'}, \overline{u'w'} - \frac{2\Omega\sin\phi}{N^2}\overline{v'\Phi_z'})\, pa\cos\phi, \tag{8}$$

where overbars denote a time mean in this section, and $\bar{u}$, $\bar{v}$, $\bar{v}^{*}$, ϕ, λ, and p denote zonal wind, meridional wind, the residual circulation of the meridional component, geopotential, longitude, and pressure, respectively. Note that the residual circulation is not equal to that used in the transformed Eulerian-mean (TEM) equations (cf. Andrews *et al.* 1987); see Miyahara (2006) for more details. The wave flux ($F_{3D}^{(\lambda)}$, $F_{3D}^{(\phi)}$, $F_{3D}^{(z)}$) is denoted in the Cartesian coordinate system as follows (x, y, and z indicate the longitude, latitude, and height, respectively):

$$(F_{3D}^{(\lambda)}, F_{3D}^{(\phi)}, F_{3D}^{(z)}) = (\hat{C}_{gx}\frac{E}{\hat{C}_x}, \hat{C}_{gy}\frac{E}{\hat{C}_x}, \hat{C}_{gz}\frac{E}{\hat{C}_x})\, pa\cos\phi, \tag{9}$$

where E denotes the kinetic plus potential energy per unit mass; $\hat{C}_x$ denotes the intrinsic zonal phase velocity; and $\hat{C}_{gx}$, $\hat{C}_{gy}$, and $\hat{C}_{gz}$ represent the zonal, meridional, and vertical intrinsic group velocities, respectively. The flux gives the wave-action density flux relative to the local time mean flow. Effects of shear from time-mean flow are neglected.

Note that the convergence (divergence) of 3-D wave activity flux corresponds to eastward (westward) wave forcing, which is opposite to the EP-flux divergence [see right side of Eq. (6); $-(\nabla g F)_{3D}$ relates to the eastward wind acceleration]. The 3-D wave flux vectors in the figures are therefore in the opposite direction to those of the EP-flux. Eastward (westward) wave forcing is illustrated as red (blue) color, as in the previous figure of EP-flux divergence. The present study investigates the zonal variation of wave forcing associated with the Kelvin waves and internal gravity waves contributing largely to driving the QBO, using the 3-D wave flux.

Because effects of shear from time-mean flow are neglected in 3-D wave flux, the first terms of $F^{(\phi)}$ and $F^{(z)}$ in the EP-flux [$\overline{v'\theta'}$ term in Eq. (3) and Eq. (4)] are not considered for the estimation of wave forcing. However, EP-flux divergence associated with $\overline{v'\theta'}$ terms is much smaller than that associated with $\overline{u'v'}$ and/or $\overline{u'w'}$ terms for internal gravity waves and Kelvin waves (not shown). Thus, the zonal-mean wave forcing calculated by 3-D wave flux divergence is confirmed to be nearly equal to that calculated by EP-flux divergence for internal gravity waves and Kelvin waves.

The $F_{3D}^{(\lambda)}$ associated with internal gravity waves and Kelvin waves is positive because $\hat{C}_x$ and $\hat{C}_{gx}$ have the same sign for these waves. The sign of $\hat{C}_{gz}$ can be known by the sign of the vertical component of energy flux ($\overline{\phi'w'} = E\hat{C}_{gz}$; because total wave energy E is always positive, the sign of $\overline{\phi'w'}$ depends on $\hat{C}_{gz}$), which is positive over wave source regions. Thus, the sign of $F_{3D}^{(z)}$ is determined by the sign of $\hat{C}_x$. When the vector direction is eastward and upward in the longitude–height plane (i.e., $F_{3D}^{(\lambda)} > 0$ and

$F_{3D}^{(z)} > 0$) over wave source regions, eastward momentum is transferred upward. In contrast, when the vector direction is eastward and downward ($F_{3D}^{(\lambda)} > 0$ and $F_{3D}^{(z)} < 0$), westward momentum is transferred upward.

Figure 6 shows longitude–height cross sections of 3-D wave flux and its divergence due to internal gravity waves and Kelvin waves in July during the eastward wind shear phase and in January during the westward wind shear phase averaged from 10°N to 10°S. Contour lines show the monthly mean zonal wind. To investigate the source distributions of Kelvin waves, the Kelvin wave filter (see Fig. 5e of part I of this paper) was applied to outgoing longwave radiation (OLR) data. We use OLR data here because the use of OLR data has been well established in detailed convectively coupled EQW studies (Kiladis *et al.* 2009 and references therein). The occurrence of convectively coupled EQWs would be a sufficient condition for the generation of EQWs with $h_e \leq 90$ m, which propagate into the stratosphere (Wheeler *et al.* 2000; Kawatani *et al.* 2009). The line graph illustrates the zonal variation in OLR variance with s $\geq$ 12 (i.e., the same spectral domains of internal gravity wave components) and with the Kelvin wave component.

First, wave forcing due to internal gravity waves is discussed. In the UTLS region, 3-D wave fluxes are strong over areas of active cumulus convection such as Africa, the Indian Ocean, and the Amazon (Figs. 6a, b). In the Eastern Hemisphere, eastward momentum is transferred upward, and strong eastward wave forcing (red color) occurs in the eastward wind shear zone associated with the Walker circulation. On the other hand, in the Western Hemisphere, westward momentum is transferred upward, and westward wave forcing (blue color) occurs in the westward wind shear zones associated

Fig.6

with the Walker circulation. These results indicate that internal gravity waves dissipate near the top of the Walker circulation and interact with background zonal wind.

In the eastward wind shear phase associated with the QBO, large eastward wave forcing due to internal gravity waves occurs in the Eastern Hemisphere around 45–25 hPa, where the mean zonal wind ranges from -12 to 6 m s^{-1} (Fig. 6a). The maximum eastward wave forcing is located around the 0 m s^{-1} line at ~35 hPa. The eastward wave forcing in the Eastern Hemisphere is much larger than that in the Western Hemisphere. The essence of this result is the same as that reported by Kawatani *et al.* (2005). On the other hand, in the westward wind shear phase, westward wave forcing around 35–20 hPa does not vary much in the zonal direction, despite slightly larger westward wave forcing in the Western Hemisphere than in the Eastern Hemisphere (Fig. 6b). Possible reasons for this are discussed in the next section. Maximum westward wave forcing occurs around -10 m s^{-1} at ~25 hPa, which is consistent with the EP-flux divergence (Fig. 2e).

Divergence of $F_{3D}^{(\lambda)}$ becomes zero in a zonal mean field [Eq. (6)]. Even when examined locally, wave forcing due to $F_{3D}^{(\lambda)}$ is much smaller than that due to $F_{3D}^{(z)}$ for internal gravity waves (not shown). As discussed in relation to Fig. 2, wave forcing due to the meridional component ($F_{3D}^{(\phi)}$) is also much smaller than that due to $F_{3D}^{(z)}$ for internal gravity waves.

Next, wave forcing due to Kelvin waves is discussed. The activities of convectively coupled Kelvin waves in the Eastern Hemisphere are larger than are those in the Western Hemisphere (line graphs in Figs. 6c, d). In the eastward wind shear phase (Fig. 6c), most Kelvin waves generated in the Eastern Hemisphere propagate upward and eastward from the troposphere into the middle stratosphere. Compared with internal

gravity waves (Fig. 6a), Kelvin waves propagate more zonally during upward propagation, resulting in more zonally elongated eastward wave forcing around 35 hPa. Much less Kelvin wave generation and propagation occur in the Western Hemisphere than in the Eastern Hemisphere. The 3-D fluxes clearly indicate that eastward wave forcing even in the eastern part of the Pacific around 35 hPa originates from Kelvin waves generated over the Indian Ocean. On the other hand, in the westward wind shear phase (Fig. 6d), most of the Kelvin waves stop propagating vertically below the maximal eastward wind of the QBO (~50 hPa).

In contrast to internal gravity waves, wave forcing due to $F_{3D}^{(\lambda)}$ associated with Kelvin waves depends greatly on the longitude around the eastward wind shear zones of the QBO (not shown). For example, in the averaged region of 60°W–130°W, 10°S–10°N, and 45–25 hPa in July (Fig. 6c), eastward wave forcing due to $F_{3D}^{(\lambda)}$ is comparable to that due to $F_{3D}^{(z)}$. On the other hand, eastward wave forcing due to $F_{3D}^{(z)}$ dominates in other longitudes. The present analysis indicates that not only vertical but also zonal convergence of wave momentum flux should be considered when wave forcing is evaluated locally.

4.2. Internal inertia-gravity wave forcing as a function of zonal phase velocity

Next, we investigate the interaction between internal gravity waves and background zonal wind in more detail. For internal gravity waves, nearly all wave forcing is due to the divergence of $F_{3D}^{(z)}$. Therefore, we calculate $F_{3D}^{(z)}$ divergence as a function of longitude and zonal phase velocity relative to the ground (C_x) along a latitudinal circle using the fast Fourier transform (FFT) described by Hayashi (1971). The longitude–time

series of $F_{3D}^{(z)}$ (x, y, z, t) (considered in Cartesian coordinates) is expressed as a longitude–C_x series of $F_{3D}^{(z)}$ (x, y, z, C_x) using this method. Here we set the resolution to $\Delta C_x = 2\,m\,s^{-1}$.

Height distributions of $F_{3D}^{(z)}$ divergence associated with internal gravity waves as a function of C_x are shown in Fig. 7 (10°S–10°N average). Because the sign of zonal wind associated with the Walker circulation changes at approximately ~180°E (Fig. 6), height distributions of $F_{3D}^{(z)}$ divergence are shown separately in the Eastern (0°–180°E) and Western (0°–180°W) hemispheres during the eastward wind and westward wind shear phase of the QBO. Monthly mean vertical profiles of zonal wind with s ≤ 11 (i.e., background zonal wind for waves with s ≥ 12) averaged in the Eastern Hemisphere/Western Hemisphere and 10°S–10°N are shown by thick solid lines. Changes of the background zonal wind in longitude, latitude, and time must influence the local propagation of internal gravity waves. The two dashed lines in the figure show the averaged zonal winds plus/minus their standard deviations (i.e., root-mean-square of longitude, latitude, and time variance of the zonal wind with s ≤ 11). Contours indicate $F_{3D}^{(z)}$ divergence with absolute values ≥ 0.01 day^{-1}, and shading represents eastward wave forcing. Note that some stratospheric wave forcing in the Western (Eastern) Hemisphere originates from waves that are generated in the troposphere in the Eastern (Western) Hemisphere and then enter the Western (Eastern) Hemisphere of the stratosphere. However, these wave propagations do not critically alter the features mentioned below (zonal propagations of internal gravity waves are shown in Figs. 6a, b).

Fig.7

First, the interaction between internal gravity waves and the Walker circulation below 120 hPa is discussed. In the Eastern Hemisphere (left panels), the westward wind associated with the Walker circulation allows most of the eastward waves with C_x of ~+10 m s^{-1} to propagate from the upper troposphere to the stratosphere, whereas most of the westward-propagating waves with C_x of ~-10 m s^{-1} are prevented from upward propagation (some westward waves with C_x of ~-10 m s^{-1} could propagate upward because of local changes in the zonal wind; see the width of the standard deviation). The situation is reversed in the Western Hemisphere (right panels). Most westward-propagating waves with C_x of ~-10 m s^{-1} are not influenced by the mean eastward wind below ~120 hPa.

Near the top of the Walker circulation around 120–80 hPa, waves with $|C_x| \leq$ ~5 m s^{-1} induce large eastward wave forcing in the Eastern Hemisphere, whereas waves with $|C_x| \leq$ ~5–10 m s^{-1} induce large westward wave forcing in the Western Hemisphere. Note that small C_x corresponds to small λz for gravity waves. The present results offer a possible reason why gravity waves with small λz have often been observed in the tropical tropopause region (e.g., Sato *et al.* 1994); internal gravity waves with small λz dominate around the tropical tropopause region due to their interaction with vertically sheared zonal wind of the Walker circulation.

Next, the interaction between internal gravity waves and the QBO around 30 hPa is investigated. In the stratosphere, C_x distributions of wave forcing are markedly related to the phase of the QBO. In the eastward wind shear phase of the QBO in the Eastern Hemisphere (Fig. 7a), waves with ~-5 m s$^{-1} \leq C_x \leq$ ~+ 20 m s^{-1} induce large eastward wave forcing around 45–25 hPa. Most eastward-propagating waves generated in the

Eastern Hemisphere do not encounter the eastward wind until ~35 hPa; as a result, most eastward waves exist until 35 hPa. On the other hand, in the eastward wind shear phase of the QBO in the Western Hemisphere (Fig. 7b), eastward wave forcing is extremely small around 45–25 hPa because eastward waves with relatively small C_x are prevented from entering the stratosphere due to upper tropospheric eastward wind.

In the westward wind shear phase of the QBO (Figs. 7c, d), waves with ~-30 m s^{-1} $\leq C_x \leq$ ~-5 m s^{-1} induce large westward wave forcing around 35–20 hPa. The difference of the altitude–C_x distribution of the westward wave forcing between the Eastern and Western hemispheres is not as obvious as in the eastward wind shear phase (see also Fig. 6b). One possible reason is that the mean upper tropospheric westward wind (solid line) in the Eastern Hemisphere is weaker in January than in July. A second possible reason is that precipitation in the equatorial region (i.e., sources of waves), which generates both eastward and westward waves, is generally greater in the Eastern Hemisphere than in the Western Hemisphere. A third reason is that the QBO westward wind is much stronger than the QBO eastward wind, "exposing" the QBO westward shear zone to a larger range of C_x in both hemispheres. Hence, the hemispheric asymmetry of wave forcing (Eastern Hemisphere vs. Western Hemisphere) is reduced compared to that of eastward waves. In summary, zonal variation of wave forcing in the equatorial stratosphere is attributed to three factors: (1) the zonal variation of wave sources in the troposphere, (2) the vertical sheared zonal winds associated the Walker circulation, and (3) the vertical wind shear of the QBO.

In the upper stratosphere above 8 hPa, eastward wave forcing with C_x of ~25 m s^{-1} is dominant in all four cases. The wave forcing is related to the eastward wind shear of

the stratopause semi-annual oscillation (SSAO) in July and the eastward wind shear of the SSAO and/or that of the upper part of the QBO in January (see Fig. 1a of part I of this paper). Because waves with C_x of ~25 m s^{-1} are not affected by the mean tropospheric wind and zonal winds of the QBO, the strength of eastward wave forcing does not differ between the Eastern and Western hemispheres as much as that of the eastward wind shear phase of the QBO. The slightly greater eastward wave forcing in the Eastern Hemisphere may result from a stronger source (line graphs in Figs. 6a, b). Study of the SSAO will be conducted in the future.

Figure 8 shows spatial distribution of 3-D wave flux divergence associated with internal gravity waves averaged over 45–25 hPa in July during the eastward wind shear phase, 35–20 hPa in January during the westward wind shear phase, and 120–80 hPa in both time periods. At 120–80 hPa in July (Fig. 8a), large eastward wave forcing is widely distributed in the Eastern Hemisphere. Eastward wave forcing from Africa to the western Pacific corresponds well to precipitation (Fig. 5c). At 120–80 hPa in January (Fig. 8b), large eastward wave forcing is located over Indonesia and the Congo Basin, associated with large precipitation (Fig. 5d). In the Western Hemisphere, westward wave forcing widely distributes in both July and January. Zonally inhomogeneous distribution of internal gravity wave forcing is apparent in the UTLS region.

At 45–25 hPa in July (Fig. 8c), large eastward wave forcing occurs from 10°S to 20°N in the Eastern Hemisphere, whereas eastward wave forcing is very weak in the Western Hemisphere, especially over the mid- to eastern Pacific. At 35–20 hPa in January (Fig. 8d), westward wave forcing elongates more zonally over the equatorial

Fig.8

region with relatively large wave forcing around Africa, Indonesia, and to the west of South America.

5. Summary and concluding remarks

This study has focused on the three-dimensional (3-D) distributions of wave forcing relevant to the QBO simulated by the T213L256 AGCM in which no gravity wave drag parameterization was included. The model well simulated convectively coupled EQWs. The choice and tuning of a cumulus convective parameterization could affect the results (see more details in part I of this study). We investigated wave forcing for two representative periods: July of the first year, during the eastward wind shear of the QBO, and January of the second year, during the westward wind shear phase (see Fig. 1a in part I). In both periods, the 0 m s^{-1} lines of the zonal wind associated with the QBO are located around 30 hPa.

First, the meridional distribution of zonal wave forcing in the zonal mean field was investigated. In both the eastward and westward wind shear phases of the QBO, nearly all EP-flux divergence due to internal gravity waves results from the divergence of the vertical component of the flux, implying that gravity wave drag parameterization including only vertical wave propagation is suitable, at least for the simulation of the QBO. On the other hand, the EP-flux divergence from the meridional component of the flux due to EQWs is comparable to that from the vertical component around the vertically sheared zonal wind of the QBO. The present analysis reveals that the distribution of wave forcing differs widely in the meridional direction.

Second, zonal variation of wave forcing associated with internal gravity waves and Kelvin waves, which contribute largely to driving the QBO, was investigated using the 3-D wave activity flux applicable to inertia-gravity waves derived by Miyahara (2006). The internal gravity waves dissipate near the top of the Walker circulation and interact with background zonal wind. In the Eastern (Western) Hemisphere, strong eastward (westward) wave forcing occurs in the eastward (westward) wind shear zone associated with the Walker circulation. Spectral analysis revealed that the strong wave forcing results from waves with small horizontal phase velocity C_x; internal gravity waves with small λz dominate around the tropical tropopause region due to interaction with the vertically sheared zonal wind associated with the Walker circulation.

Around the altitude of the eastward wind shear of the QBO, the eastward wave forcing due to internal gravity waves in the Eastern Hemisphere is much larger than that in the Western Hemisphere. On the other hand, in the westward wind shear phase, westward wave forcing does not vary much in the zonal direction. Three factors produce the zonal variation of the wave forcing distribution in the stratosphere: (1) the zonal variation of wave sources in the troposphere, (2) the vertically sheared zonal winds associated with the Walker circulation, and (3) the vertical wind shear of the QBO.

In the upper troposphere, more Kelvin waves are generated in the Eastern Hemisphere than in the Western Hemisphere due to the larger activities of convectively coupled Kelvin waves in the Eastern Hemisphere (Kawatani *et al.* 2009). Compared with internal gravity waves, Kelvin waves propagate more zonally during upward propagation, resulting in more zonally elongated eastward wave forcing, apart from the source region in the eastward wind shear of the QBO.

The present study clearly illustrates the zonal variation of wave momentum flux and wave forcing and suggests that the wave momentum flux observed at Singapore (Sato and Dunkerton 1997) would be stronger than values at other longitudes (Figs. 1 and 6). At present, radiosonde stations conducting routine observations in the tropics are located mainly on land. Therefore, not enough observations of small-scale waves are available to verify the realism of the forcing by simulated internal gravity waves. Observations at many different locations near the equator are desired to investigate the roles of waves in driving the QBO in the real atmosphere.

Finally, we discuss the shorter period of simulated QBO in this experiment. The net and absolute values of simulated wave momentum fluxes ($\overline{u'w'}$ and $|\overline{u'w'}|$) were compared with rawinsonde observations from Singapore (Sato and Dunkerton 1997). The momentum fluxes with eastward internal gravity waves and Kelvin waves were confirmed to be reasonably simulated, whereas those due to westward internal gravity waves would be slightly overestimated (Fig. 1). The EP-flux divergence of all components shows that westward wave forcing during westward wind shear is comparable to eastward wave forcing during eastward wind shear (see Fig. 1a of part I of this paper). The simulated downward-propagating phase speed in the westward wind shear is also comparable to that in the eastward wind shear in the present model, whereas the speed in the westward wind shear is slower than that in the eastward wind shear in the real atmosphere. These results suggest the possibility that the shorter period of the simulated QBO might result from (1) underrepresentation of $\overline{w}^*$ in the tropics, as illustrated in part I of this paper, and (2) relatively larger wave momentum flux, especially associated with westward gravity waves. The zonal wavenumber / frequency

spectra of simulated precipitation reveals that the westward component with s ≥ 12 is relatively overestimated compared to the eastward component (Fig. 4 of part I of this paper), which would be one reason for the overestimation of westward waves.

This study analyzed the outputs of an AGCM integrated for 3 years with a climatological boundary condition. In the real atmosphere, wave forcing might show distinct interannual variation associated with tropospheric variability, such as El Niño–Southern Oscillation (ENSO) events. To investigate interannual variation of wave forcing in the model, analysis over longer periods is required. Further studies using the AGCM and other models in conjunction with observations are required to better understand global wave activities and their roles in the middle atmosphere.

References

Alexander, S. P., T. Tsuda, and Y. Kawatani, 2008a: COSMIC GPS observations of Northern Hemisphere winter stratospheric gravity waves and comparisons with an atmospheric general circulation model, *Geophys. Res. Lett*., **35**, L10808, doi:10.1029/2008GL033174.

Alexander, S. P., T. Tsuda, Y. Kawatani, and M. Takahashi, 2008b: Global distribution of atmospheric waves in the equatorial upper troposphere and lower stratosphere: COSMIC observations of wave mean flow interactions, *J. Geophys. Res*., **113**, D24115, doi:10.1029/2008JD010039.

Andrews, D. G., and M. E. McIntyre, 1976: Planetary waves in horizontal and vertical shear: The generalized Eliassen–Palm relation and the mean zonal acceleration, *J. Atmos. Sci.*, **33**, 2031–2048.

Andrews, D. G., J. R. Holton, and C. B. Leovy, 1987: Middle Atmosphere Dynamics, *Academic Press*, 489 pp.

Baldwin, M. P., L. J. Gray, T. J. Dunkerton, K. Hamilton, P. H. Haynes, W. J. Randel, J. R. Holton, M. J. Alexander, I. Hirota, T. Horinouchi, D. B. A. Jones, J. S. Kinnersley, C. Marquardt, K. Sato, and M. Takahashi, 2001: The quasi-biennial oscillation, *Rev. of Geophys.*, **39**, 179–229.

Bergman, J. W., and M. L. Salby, 1994: Equatorial wave activity derived from fluctuations in observed convection, *J. Atmos. Sci.*, **51**, 3791–3806.

Ern, M., and P. Preusse, 2009: Wave fluxes of equatorial Kelvin waves and QBO zonal wind forcing derived from SABER and ECMWF temperature space-time spectra, *Atmos. Chem. Phys*., **9**, 3957–3986

Ern, M., P. Preusse, M. Krebsbach, M. G. Mlynczak, and J. M. Russell, III, 2008: Equatorial wave analysis from SABER and ECMWF temperatures, *Atmos. Chem. Phys.*, **8**, 845–869.

Gill, A. E., 1982: *Atmospheric-Ocean Dynamics*, Academic Press, New York, 662 pp.

Giorgetta, M. A., E. Manzini, and E. Roechner, 2002: Forcing of the quasi-biennial oscillation from a broad spectrum of atmospheric waves, *Geophys. Res. Lett*., **29**, 1245, doi:10.1029/2002GL014756.

Giorgetta, M. A., E. Manzini, E. Roechner, M. Esch, and L. Bengtsson, 2006: Climatology and forcing of the quasi-biennial oscillation in the MAECHAM5 model, *J. Climate*, **19**, 3882–3901.

Hamilton, K., A. Hertzog, F. Vial, and G. Stenchikov, 2004: Longitudinal variation of the stratospheric quasi-biennial oscillation, *J. Atmos. Sci.*, **61**, 383–402.

Hayashi, Y., 1971: A generalized method of resolving disturbances into progressive and retrogressive waves by space Fourier and time cross-spectral analysis, *J. Meteorol. Soc. Jpn.*, **49**, 125-128

Imamura, T., 2006: Meridional propagation of planetary-scale waves in vertical shear: Implication for the Venus atmosphere, *J. Atmos. Sci.*, **63**, 1623–1636.

Kawatani, Y., S. K. Dhaka, M. Takahashi, and T. Tsuda, 2003: Large potential energy of gravity waves over a smooth surface with little convection, *Geophys. Res. Lett.*, **30**(8), 1438, doi:10.1029/2003GL016960.

Kawatani, Y., M. Takahashi, and T. Tokioka, 2004: Gravity waves around the subtropical jet of the southern winter in an atmospheric general circulation model, *Geophys. Res. Lett*., **31**, L22109, doi:10.1029/2004GL020794.

Kawatani, Y., K. Tsuji, and M. Takahashi, 2005: Zonally non-uniform distribution of equatorial gravity waves in an atmospheric general circulation model, *Geophys. Res. Lett.*, **32**, L23815, doi:10.1029/2005GL024068.

Kawatani, Y., M. Takahashi, K. Sato, S. P. Alexander, and T. Tsuda, 2009: Global distribution of atmospheric waves in the equatorial upper troposphere and lower stratosphere: AGCM simulation of sources and propagation, *J. Geophys. Res.*, **114**, D01102, doi:10.1029/2008JD010374.

Kawatani, Y., K. Sato, D. J. Dunkerton, S. Watanabe, S. Miyahara, and M. Takahashi, 2010: The roles of equatorial trapped waves and internal inertia-gravity waves in driving the quasi-biennial oscillation. Part I: zonal mean wave forcing, *J. Atmos. Sci., submitted*

Kiladis, G. N., M. C. Wheeler, P. T. Haertel, K. H. Straub, P. E. Roundy, 2009: Convectively coupled equatorial waves, *Rev. Geophys.*, **47**, RG2003, doi:10.1029/2008RG000266.

Maruyama, T., 1994: Upward transport of eastward wind momentum due to disturbances of the equatorial lower stratosphere in the period range of about 2 days—Singapore data analysis for 1983–1993, *J. Meteorol. Soc. Jpn.*, **72**, 423–432.

McLandress, C., 1998: On the importance of gravity waves in the middle atmosphere and their parameterization in general circulation models, *J. Atmos. Solar-Terr. Phys.*, **60**, 1357–1383.

Miyahara, S., 2006: A three-dimensional wave activity flux applicable to inertio-gravity waves, *SOLA*, **2**, 108–111.

Randel, W. J., and F. Wu, 2005: Kelvin wave variability near the equatorial tropopause observed in GPS radio occultation measurements, *J. Geophys. Res.*, **110**, doi:10.1029/2004JD005006.

Ratnam, M. V., G. Tetzlaff, and C. Jacobi, 2004: Global and seasonal variations of stratospheric gravity wave deduced from the CHAMP/GPS satellite, *J. Atmos. Sci.*, **61**, 1610–1620.

Sato, K., and T. J. Dunkerton, 1997: Estimates of momentum flux associated with equatorial Kelvin and gravity waves, *J. Geophys. Res.*, **102**, 26,247–26,261.

Sato, K., F. Hasegawa, and I. Hirota, 1994: Short-period disturbances in the equatorial lower stratosphere, *J. Meteor. Soc. Japan*, **72**, 859–872.

Sato, K., T. Kumakura, and M. Takahashi, 1999: Gravity waves appearing in a high resolution GCM simulation, *J. Atmos. Sci.*, **56**, 1005–1018.

Sato, K., S. Watanabe, Y. Kawatani, Y. Tomikawa, K. Miyazaki, and M. Takahashi, 2009: On the origins of mesospheric gravity waves, *Geophys. Res. Lett.*, **36**, L19801, doi:10.1029/2009GL039908.

Tindall, J. C., J. Thuburn, and E. J. Highwood, 2006a: Equatorial waves in the lower stratosphere. I: A novel detection method, *Q. J. R. Meteorol. Soc.*, **132**, 177–194, doi:10.1256/qj.04.152, 2006a.

Tindall, J. C., J. Thuburn, and E. J. Highwood, 2006b: Equatorial waves in the lower stratosphere. II: Annual and interannual variability, *Q. J. R. Meteorol. Soc.*, **132**, 195–212, doi:10.1256/qj.04.153, 2006b.

Tsuda, T., Y. Murayama, H. Wiryosumarto, S. W. B. Harijono, and S. Kato, 1994: Radiosonde observations of equatorial atmosphere dynamics over Indonesia, 2, Characteristics of gravity waves, *J. Geophys. Res*., **99**, 10,507–10,516.

Tsuda, T., M. Nishida, C. Rocken, and R. H. Ware, 2000: A global morphology of gravity wave activity in the stratosphere revealed by the GPS occultation data (GPS/MET), *J. Geophys. Res*., **105**, 7257–7273.

Tsuda, T., M. V. Ratnam, S. P Alexander, T. Kozu, and Y. Takayabu, 2009: Temporal and spatial distributions of atmospheric wave energy in the equatorial stratosphere revealed by GPS radio occultation temperature data obtained with the CHAMP Satellite during 2001–2006, *Earth Planets Space*, **61**, 525–533.

Wada, K., T. Nitta, and K. Sato, 1999: Equatorial inertia-gravity waves in the lower stratosphere revealed by TOGA-COARE IOP data, *J. Meteor. Soc. Japan*, **77**, 721–736.

Watanabe, S., 2008: Constraints on a non-orographic gravity wave drag parameterization using a gravity wave resolving general circulation model, *SOLA*, **4**, 61–64.

Watanabe S., T. Nagashima, and S. Emori, 2005: Impact of global warming on gravity wave momentum flux in the lower stratosphere, *SOLA*, **1**, 189–192.

Watanabe, S., K. Sato, and M. Takahashi, 2006: A general circulation model study of orographic gravity waves over Antarctica excited by katabatic winds, *J. Geophys. Res*., **111**, D18104, doi:10.1029/2005JD006851.

Watanabe, S., Y. Kawatani, Y. Tomikawa, K. Miyazaki, M. Takahashi, and K. Sato, 2008: General aspects of a T213L256 middle atmosphere general circulation model, *J. Geophys. Res*., **113**, D12110, doi:10.1029/2008JD010026.

Wheeler, M., G. N. Kiladis, and P. J. Webster, 2000: Large-scale dynamical fields associated with convectively coupled equatorial waves, *J. Atmos. Sci.*, **57**, 613–640.

Xie, P., and P. A. Arkin, 1996: Analyses of global monthly precipitation using gauge observations, satellite summaries, and numerical model predictions, *J. Climate*, **9**, 840-858.

List of Figures

Fig. 1: Longitude–height cross section of (a, b) net $\overline{u'w'} \leq 3$ day and (c, d) the absolute value of $|\overline{u'w'}| \leq 3$ day in (a, c) July during the eastward wind shear and (b, d) in January during the westward wind shear phase of the QBO (3°S–3°N average). Zonal wind is contoured. The dashed vertical line indicates the location of Singapore at 104°E. The contour interval is 5 m s^{-1}. The solid and dashed lines indicate eastward wind and westward wind, respectively. The bold line corresponds to 0 m s^{-1} for zonal wind.

Fig. 2: Latitude–height cross section of the EP-flux and its divergence due to (a, d) s ≤ 11 and due to (b, e) internal gravity waves in (a–c) July during the eastward wind shear phase and (d–f) January during the westward wind shear phase of the QBO. Red and blue colors for (a, b, d, e) correspond to eastward and westward wave forcing, respectively. Zonal-mean zonal wind is indicated by contours. The arrow units are 1.5 x 10^6 Kg s^{-2}. The color interval is 0.1 m s^{-1} day^{-1}. The contour interval is 5 m s^{-1}. The vertical component of the EP-flux is multiplied by a factor of 420. (c, f) Vertical profile of EP-flux divergence due to s ≤ 11 of meridional (blue) and vertical (green) components and that due to internal gravity waves of meridional (yellow) and vertical (red) components averaged from 10°S to 10°N.

Fig. 3: Latitude–height cross section of (a–c) the EP-flux and its divergence, EP-flux divergence from the (d–f) meridional component and (g–i) vertical component of the flux due to (a, d, g) Kelvin waves and (b, e, h) n = 0 EIGWs in July during the eastward wind shear phase and (c, f, i) MRG waves in January during the westward wind shear phase of

the QBO. Red and blue colors correspond to eastward and westward wave forcing, respectively. Zonal-mean zonal wind is contoured. The arrow unit is 8×10^5 Kg s^{-2} for (a), 2×10^5 Kg s^{-2} for (b), and 1.5×10^5 Kg s^{-2} for (c). The color interval is 0.6×10^{-1} m s^{-1} day^{-1} for (a, d, g) and 0.2×10^{-1} m s^{-1} day^{-1} for (b, c, e, f, h, i). The contour interval is 5 m s^{-1}. The vertical component of EP-flux is multiplied by a factor of 420.

Fig. 4: Latitudinal distribution of EP-flux divergence (a) at 45–25 hPa in July during the eastward wind shear phase and (b) at 35–20 hPa in January during the westward wind shear phase of the QBO. Lines marked A indicate EP-flux divergence due to (a) Kelvin waves and n = 1 EIGWs and (b) n = 1 and n = 2 equatorial Rossby waves. Lines marked B show (a) n = 0 and n = 2 EIGWs and (b) MRG waves. Lines marked C correspond to (a) the sum of eastward EQWs and (b) n = 1 and n = 2 WIGWs. Lines marked D and E show large-scale non-EQWs (see text) and internal gravity waves, respectively.

Fig. 5: Distribution of precipitation (mm day^{-1}) in (a, c) July and (b, d) January obtained by (a, b) CMAP data and (c, d) the model. The CMAP data were averaged from 1979 to 2001, whereas the model data were for 1 month: (c) July of the first year and (d) January of the second year. The shaded interval is 2 mm day^{-1}; values ≥2 mm day^{-1} are shown.

Fig. 6: Longitude–height cross sections of (vectors) 3-D wave activity flux and its divergence due to (a, b) internal gravity waves and (c, d) Kelvin waves in (a, c) July during the eastward wind shear phase and in (b, d) January during the westward wind shear phase (10°N–10°S average). Note that the convergence (divergence) of 3-D wave

activity flux corresponds to eastward (westward) wave forcing, which is opposite to the EP-flux divergence. The wave flux vectors in the figures appear opposite to those of the EP-flux. Red and blue colors correspond to eastward and westward wave forcing, respectively. The 3-D wave activity flux is divided by pressure P so that the arrows in the stratosphere may more easily be seen. Contour lines show the zonal wind. The arrow unit is 6.0 x 10^7 (m^3 s^2) and fluxes $\geq$2.0 x 10^7 (m^3 s^2) are drawn. The vertical component of 3-D wave flux is multiplied by a factor of 1000. The color interval is 1.0 x 10^{-1} m s^{-1} day^{-1} with absolute values $\geq$1.0 x 10^{-1} m s^{-1} day^{-1} drawn for (a, b) and 0.5 x 10^{-1} m s^{-1} day^{-1} with absolute values $\geq$0.5 x10^{-1} m s^{-1} day^{-1} drawn for (c, d). The contour interval is 5 m s^{-1} for zonal wind. Solid and dashed lines correspond to eastward and westward wind, respectively. The bold solid lines indicate the 0 m s^{-1} line of the zonal wind. The line graph below each figure indicates the zonal variation in OLR variance (W^2 m^{-4}) due to (a, b) internal gravity waves and (c, d) Kelvin wave components (10°S–10°N mean). Note that the color interval of (a, b) is two times that of (c, d); also note the different ranges of the ordinate axes of OLR for internal gravity waves and Kelvin waves.

Fig. 7: Height distributions of $F_{3D}^{(z)}$ divergence (i.e., zonal wave forcing) due to internal gravity waves as a function of the zonal phase velocity relative to the ground C_x in (a, b) July during the eastward wind shear and in (c, d) January during the westward wind shear phase of the QBO. The left (right) figures are zonally averaged in the Eastern (Western) Hemisphere. The contour interval is 0.01 day^{-1} and values $\leq$-0.01 day^{-1} (eastward wave forcing) are shaded. Monthly mean vertical profiles of the zonal wind with s $\leq$ 11 averaged zonally in the (left) Eastern Hemisphere and (right) Western Hemisphere and

meridionally from 10°S–10°N are indicated by thick solid lines; the two dashed lines represent averaged zonal wind plus/minus the standard deviation. See text for details.

Fig. 8: Spatial distribution of 3-D wave activity flux divergence due to internal gravity waves at (a, b) 120–80 hPa, (c) 45–25 hPa, and (d) 35–20 hPa in (left) July during the eastward wind shear phase and (right) January during the westward wind shear phase. Red and blue colors correspond to eastward and westward wave forcing, respectively. The color interval is 3.0×10^{-1} m s^{-1} day^{-1} for (a, b) and 1.0×10^{-1} m s^{-1} day^{-1} for (c, d). Zonal wind is contoured with a contour interval of 5 m s^{-1}. Solid and dashed lines correspond to eastward and westward wind, respectively. The bold solid lines indicate the 0 m s^{-1} line of the zonal wind.
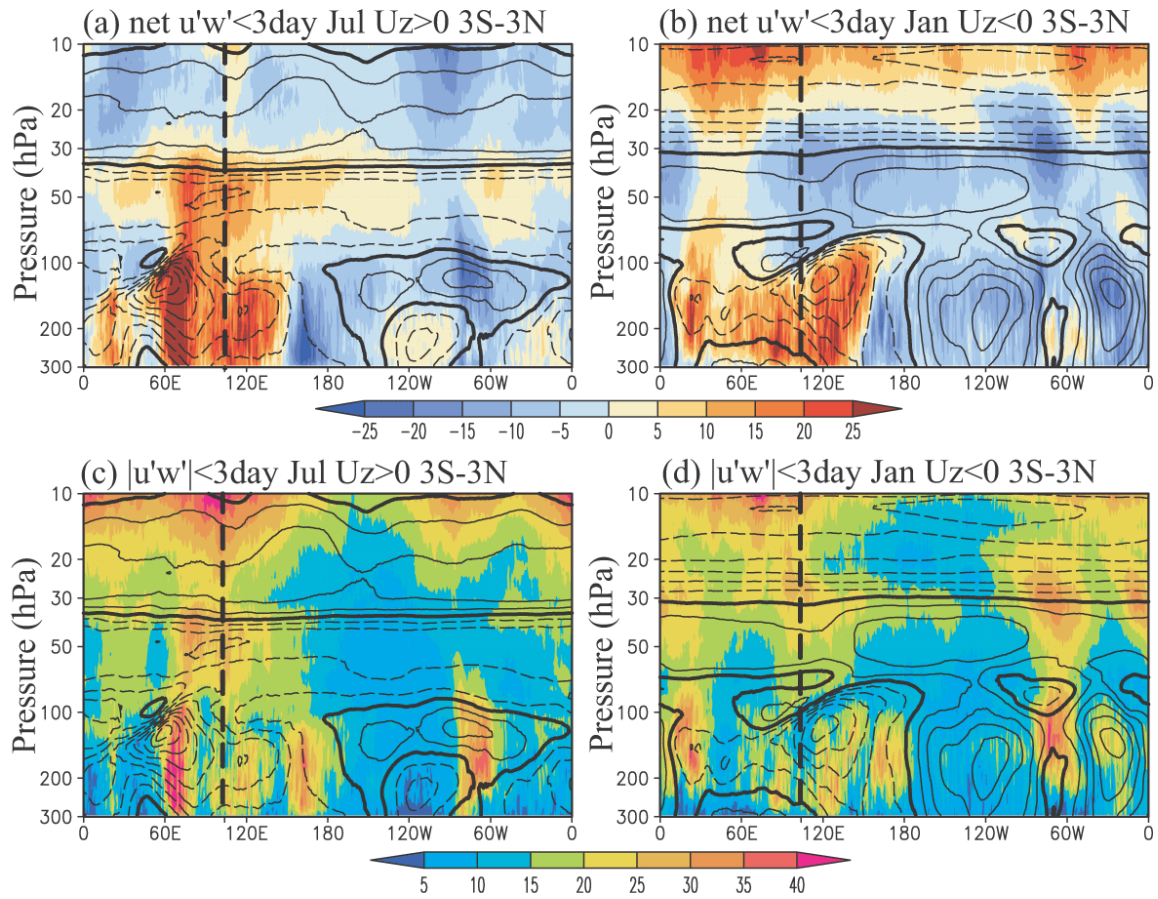
Fig. 1

Fig. 1: Longitude–height cross section of (a, b) net $\overline{u'w'} \leq 3$ day and (c, d) the absolute value of $|\overline{u'w'}| \leq 3$ day in (a, c) July during the eastward wind shear and (b, d) in January during the westward wind shear phase of the QBO (3°S–3°N average). Zonal wind is contoured. The dashed vertical line indicates the location of Singapore at 104°E. The contour interval is 5 m s^{-1}. The solid and dashed lines indicate eastward wind and westward wind, respectively. The bold line corresponds to 0 m s^{-1} for zonal wind.

Fig. 2

Fig. 2: Latitude–height cross section of the EP-flux and its divergence due to (a, d) s ≤ 11 and due to (b, e) internal gravity waves in (a–c) July during the eastward wind shear phase and (d–f) January during the westward wind shear phase of the QBO. Red and blue colors for (a, b, d, e) correspond to eastward and westward wave forcing, respectively. Zonal-mean zonal wind is indicated by contours. The arrow units are 1.5×10^6 Kg s^{-2}. The color interval is 0.1 m s^{-1} day^{-1}. The contour interval is 5 m s^{-1}. The vertical component of the EP-flux is multiplied by a factor of 420. (c, f) Vertical profile of EP-flux divergence due to s ≤ 11 of meridional (blue) and vertical (green) components and that due to internal gravity waves of meridional (yellow) and vertical (red) components averaged from 10°S to 10°N.
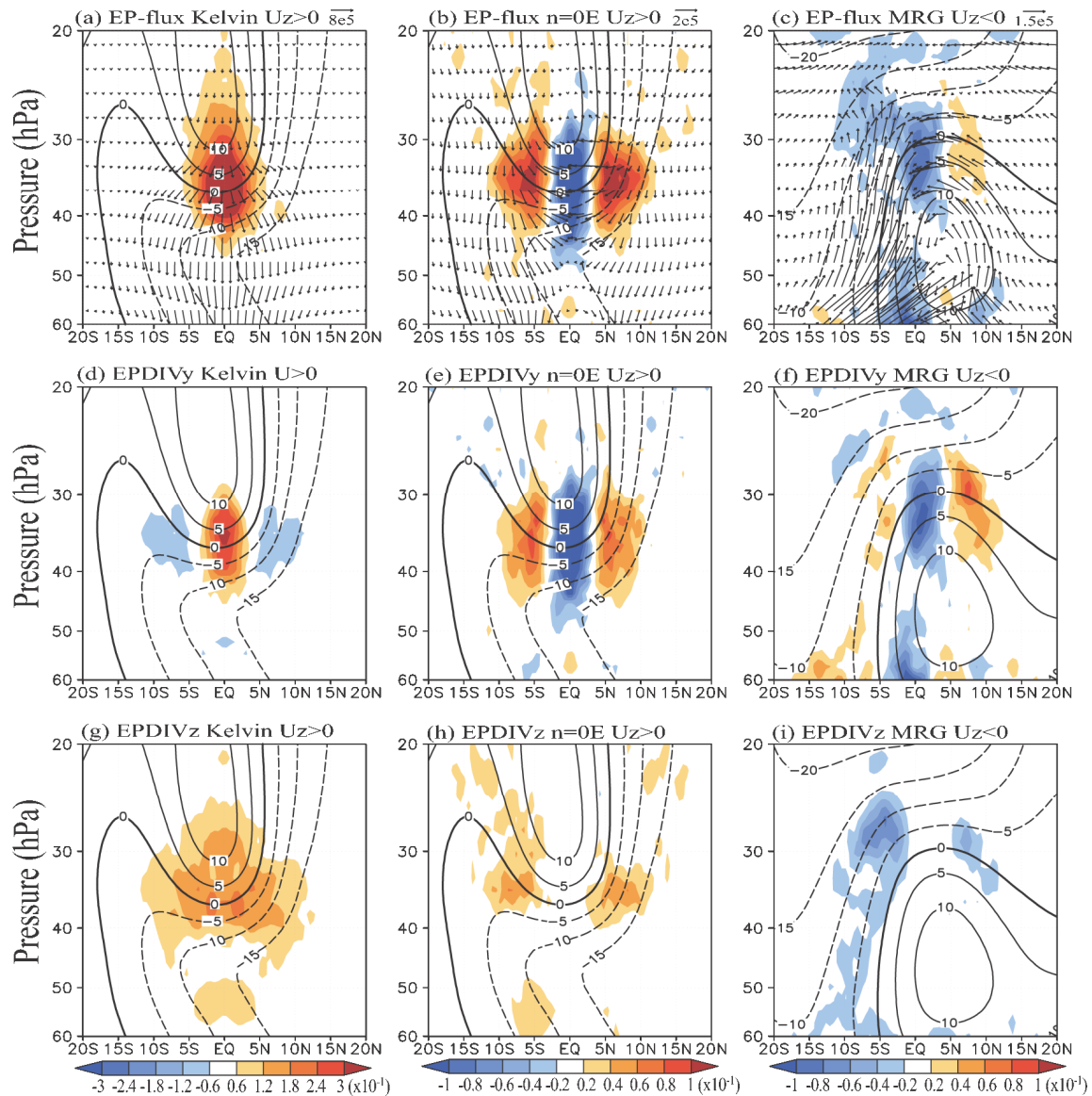
Fig. 3

Fig. 3: Latitude–height cross section of (a–c) the EP-flux and its divergence, EP-flux divergence from the (d–f) meridional component and (g–i) vertical component of the flux due to (a, d, g) Kelvin waves and (b, e, h) $n = 0$ EIGWs in July during the eastward wind shear phase and (c, f, i) MRG waves in January during the westward wind shear phase of the QBO. Red and blue colors correspond to eastward and westward wave forcing, respectively. Zonal-mean zonal wind is contoured. The arrow unit is 8×10^5 Kg s^{-2} for (a), 2×10^5 Kg s^{-2} for (b), and 1.5×10^5 Kg s^{-2} for (c). The color interval is 0.6×10^{-1} m s^{-1} day^{-1} for (a, d, g) and 0.2×10^{-1} m s^{-1} day^{-1} for (b, c, e, f, h, i). The contour interval is 5 m s^{-1}. The vertical component of EP-flux is multiplied by a factor of 420.
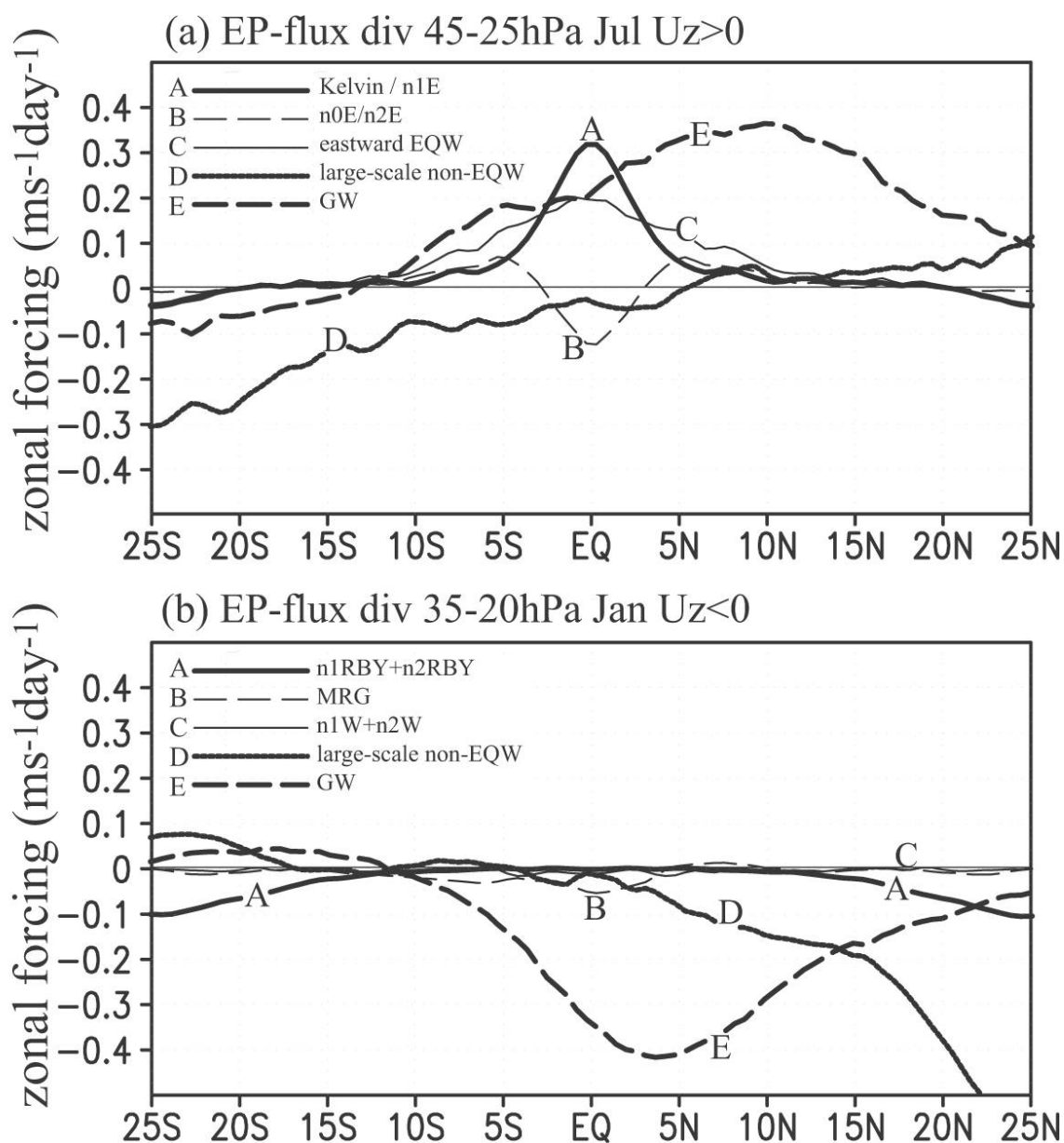
Fig. 4

Fig. 4: Latitudinal distribution of EP-flux divergence (a) at 45–25 hPa in July during the eastward wind shear phase and (b) at 35–20 hPa in January during the westward wind shear phase of the QBO. Lines marked A indicate EP-flux divergence due to (a) Kelvin waves and n = 1 EIGWs and (b) n = 1 and n = 2 equatorial Rossby waves. Lines marked B show (a) n = 0 and n = 2 EIGWs and (b) MRG waves. Lines marked C correspond to (a) the sum of eastward EQWs and (b) n = 1 and n = 2 WIGWs. Lines marked D and E show large-scale non-EQWs (see text) and internal gravity waves, respectively.
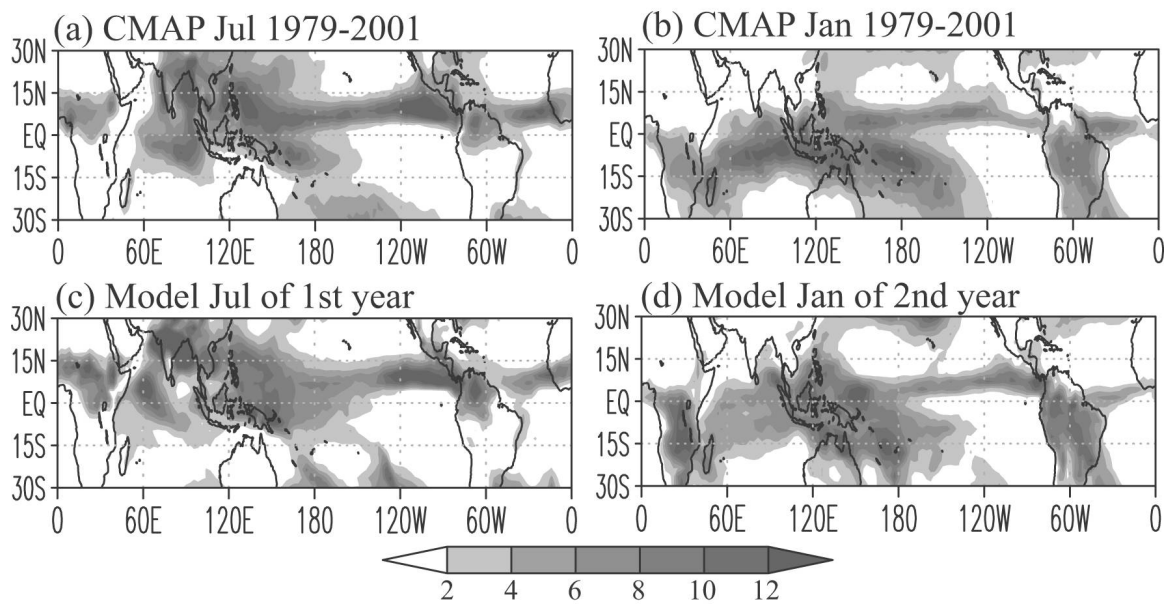
Fig. 5

Fig. 5: Distribution of precipitation (mm day^{-1}) in (a, c) July and (b, d) January obtained by (a, b) CMAP data and (c, d) the model. The CMAP data were averaged from 1979 to 2001, whereas the model data were for 1 month: (c) July of the first year and (d) January of the second year. The shaded interval is 2 mm day^{-1}; values ≥ 2 mm day^{-1} are shown.
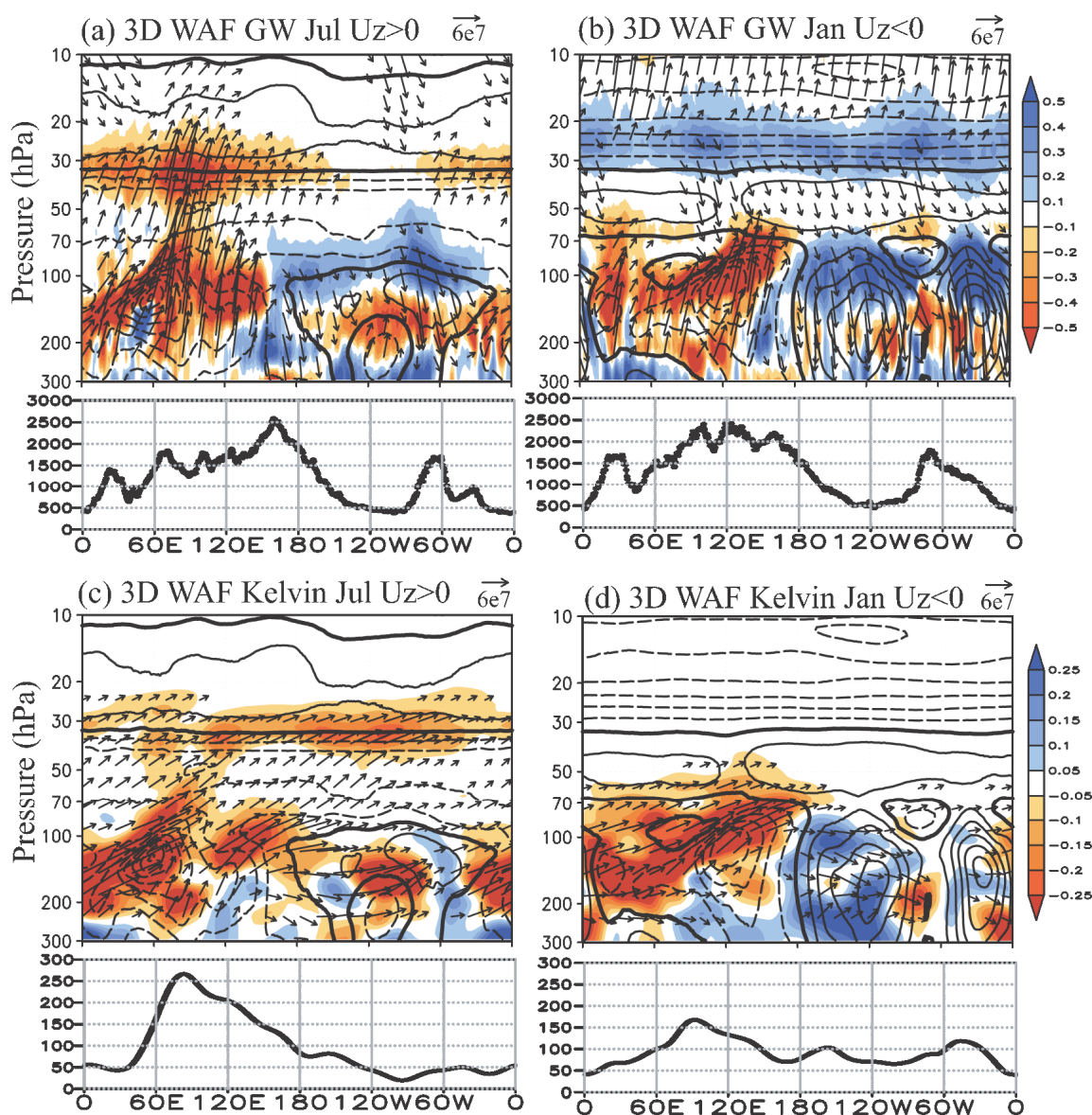
Fig. 6: Longitude–height cross sections of (vectors) 3-D wave activity flux and its divergence due to (a, b) internal gravity waves and (c, d) Kelvin waves in (a, c) July during the eastward wind shear phase and in (b, d) January during the westward wind shear phase (10°N–10°S average). Note that the convergence (divergence) of 3-D wave activity flux corresponds to eastward (westward) wave forcing, which is opposite to the EP-flux divergence. The wave flux vectors in the figures appear opposite to those of the EP-flux. Red and blue colors correspond to eastward and westward wave forcing, respectively. The 3-D wave activity flux is divided by pressure P so that the arrows in the stratosphere may more easily be seen. Contour lines show the zonal wind. The arrow unit

is 6.0 x 10^7 (m^3 s^2) and fluxes ≥2.0 x 10^7 (m^3 s^2) are drawn. The vertical component of 3-D wave flux is multiplied by a factor of 1000. The color interval is 1.0 x 10^{-1} m s^{-1} day^{-1} with absolute values ≥1.0 x 10^{-1} m s^{-1} day^{-1} drawn for (a, b) and 0.5 x 10^{-1} m s^{-1} day^{-1} with absolute values ≥0.5 x10^{-1} m s^{-1} day^{-1} drawn for (c, d). The contour interval is 5 m s^{-1} for zonal wind. Solid and dashed lines correspond to eastward and westward wind, respectively. The bold solid lines indicate the 0 m s^{-1} line of the zonal wind. The line graph below each figure indicates the zonal variation in OLR variance (W^2 m^{-4}) due to (a, b) internal gravity waves and (c, d) Kelvin wave components (10°S–10°N mean). Note that the color interval of (a, b) is two times that of (c, d); also note the different ranges of the ordinate axes of OLR for internal gravity waves and Kelvin waves.

Fig. 7

Eastern Hemisphere   *Western Hemisphere*

(a) GW forcing 0-180E Jul   (b) GW forcing 0-180W Jul

(c) GW forcing 0-180E Jan   (d) GW forcing 0-180W Jan

Eastward wind shear

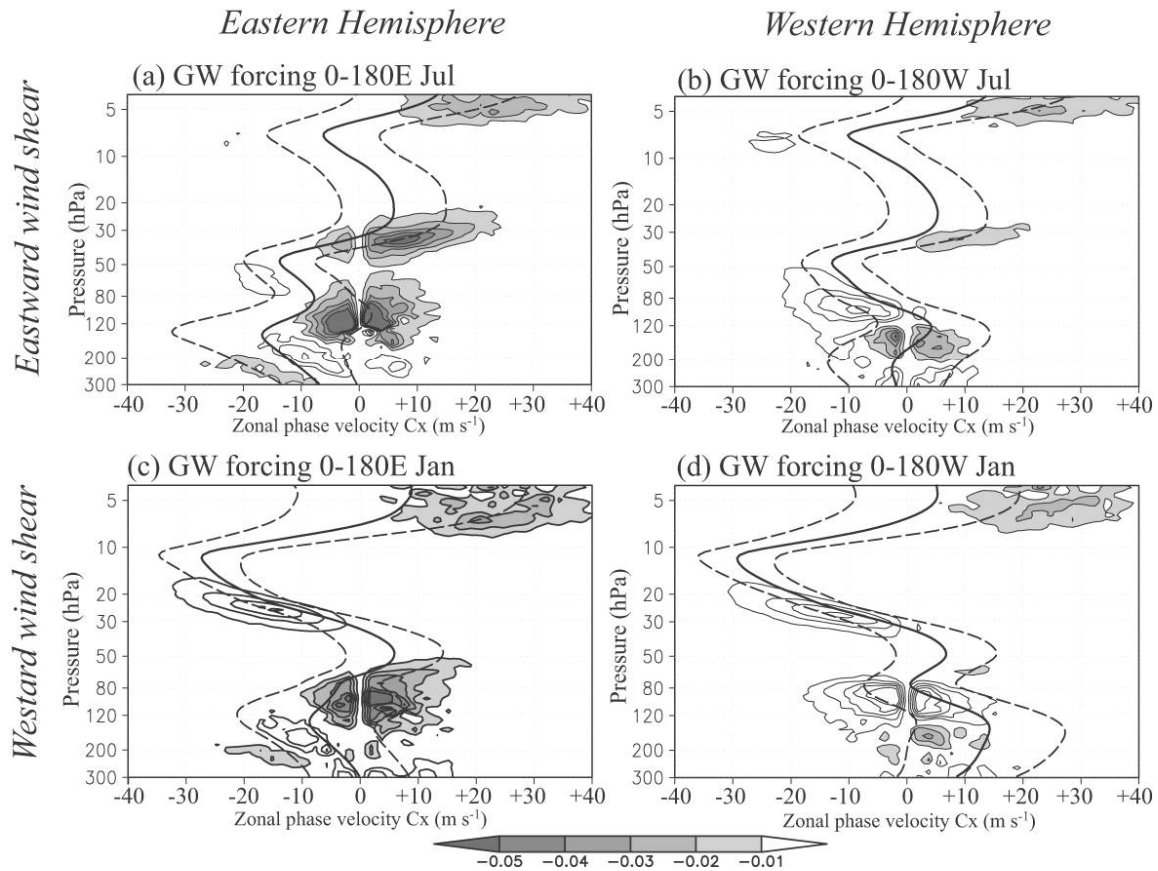*Westard wind shear*

−0.05 −0.04 −0.03 −0.02 −0.01

Fig. 7: Height distributions of $F_{3D}^{(z)}$ divergence (i.e., zonal wave forcing) due to internal gravity waves as a function of the zonal phase velocity relative to the ground C_x in (a, b) July during the eastward wind shear and in (c, d) January during the westward wind shear phase of the QBO. The left (right) figures are zonally averaged in the Eastern (Western) Hemisphere. The contour interval is 0.01 day^{-1} and values $\leq$-0.01 day^{-1} (eastward wave forcing) are shaded. Monthly mean vertical profiles of the zonal wind with $s \leq 11$ averaged zonally in the (left) Eastern Hemisphere and (right) Western Hemisphere and meridionally from 10°S–10°N are indicated by thick solid lines; the two dashed lines represent averaged zonal wind plus/minus the standard deviation. See text for details.

Fig.8

(a) GW 3-D flux div Jul 120-80hPa

(b) GW 3-D flux div Jan 120-80hPa

−1.5 −1.2 −0.9 −0.6 −0.3 0 0.3 0.6 0.9 1.2 1.5

(c) GW 3-D flux div Jul 45-25hPa

(d) GW 3-D flux div Jan 35-20hPa

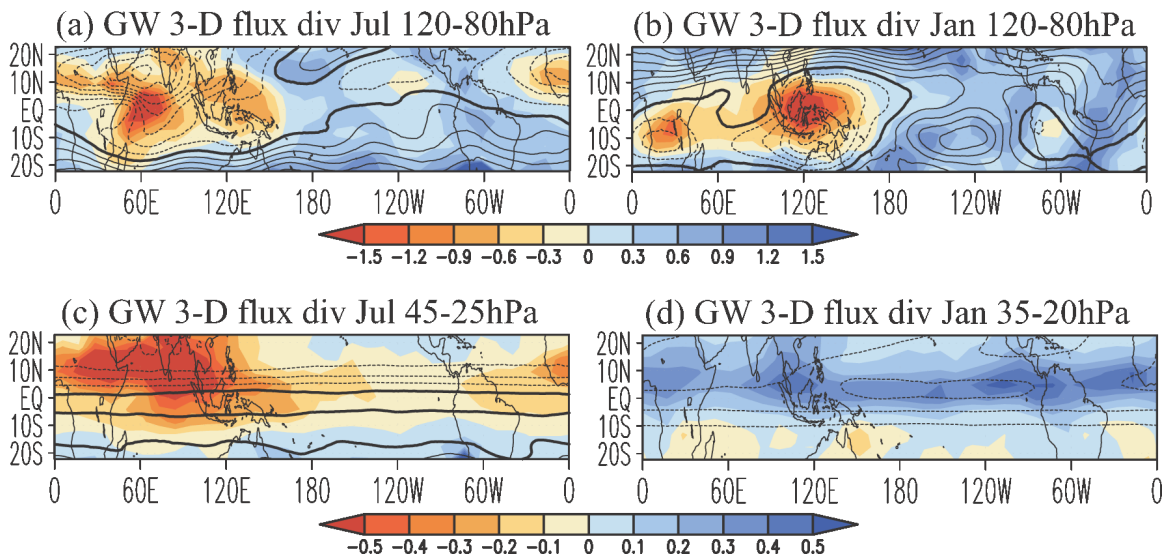−0.5 −0.4 −0.3 −0.2 −0.1 0 0.1 0.2 0.3 0.4 0.5

Fig. 8: Spatial distribution of 3-D wave activity flux divergence due to internal gravity waves at (a, b) 120–80 hPa, (c) 45–25 hPa, and (d) 35–20 hPa in (left) July during the eastward wind shear phase and (right) January during the westward wind shear phase. Red and blue colors correspond to eastward and westward wave forcing, respectively. The color interval is 3.0×10^{-1} m s^{-1} day^{-1} for (a, b) and 1.0×10^{-1} m s^{-1} day^{-1} for (c, d). Zonal wind is contoured with a contour interval of 5 m s^{-1}. Solid and dashed lines correspond to eastward and westward wind, respectively. The bold solid lines indicate the 0 m s^{-1} line of the zonal wind.